

# Studying the global dynamics of conservative dynamical systems using the SALI chaos detection method

T. M. Aros<sup>x</sup>, Ch. Skokos<sup>z</sup>, E. A. Thanassoulas<sup>y</sup> and T. Bountis

Center for Research and Applications of Nonlinear Systems (CRANS), Department of Mathematics, University of Patras, GR-26500, Greece.

<sup>x</sup> Observatoire Astronomique de Marseille-Provence (OAMP), 2 Place Le Verrier, F-13248, Marseille, France.

<sup>y</sup> Astronomie et Systèmes Dynamiques, Institut de Mécanique Céleste et de Calcul des Éphémérides (IMCCE), Observatoire de Paris, 77 avenue Denfert-Rochereau, F-75014, Paris, France.

**Abstract.** We use the Smaller Alignment Index (SALI) method of chaos detection, to study the global dynamics of conservative dynamical systems described by differential or difference equations. In particular, we consider the well-known 2 and 4-dimensional symplectic standard map, as well as an autonomous Hamiltonian system of 2 and 3 degrees of freedom describing the motion of a star in models of barred galaxies. The application of SALI helped us to compute rapidly and accurately the percentage of regular and chaotic motion for particular values of the parameters of these systems. We were also able to perform a computationally efficient determination of the dependence of these percentages on the variation of several parameters of the studied models.

**Keywords:** Symplectic maps, Hamiltonian systems, Standard map, Barred galactic potentials, Chaotic motion, Regular motion, SALI method

## 1 Introduction

The qualitative distinction between chaotic and regular motion in symplectic maps and in systems of differential equations is a fundamental problem of nonlinear dynamics. This distinction is in general, a non trivial task and it becomes more difficult as the number of degrees of freedom increases. For this reason, over the years, several methods distinguishing regular from chaotic motion in conservative dynamical systems have been proposed and applied, with varying degrees of success.

One of the most efficient methods of chaos detection is the computation of the so-called Smaller Alignment Index (SALI) which was introduced in [1] and has already been applied successfully to several dynamical systems [1-18]. SALI has proved to be a fast and reliable method which can distinguish between regular and chaotic motion rapidly, reliably and accurately. These characteristics make this index perfectly suited for the study of global dynamics of dynamical systems. For these reasons we use the SALI to study the behavior of two distinct dynamical systems: the well-known 2-dimensional (2D) standard map [19] and its generalization to higher dimensions, as well as Hamiltonian systems of 2 (2D) and 3 (3D) degrees of freedom, describing the motion of stars in models of barred galaxies. In the present paper, we present some preliminary results of our studies.

The paper is organized as follows: In Section 2 we recall the definition of SALI explaining also its behavior for regular and chaotic orbits. In Section 3 we use SALI for computing the fraction of chaotic orbits in the case of the standard map, while in Section 4 the results of an analogous study for Hamiltonian systems of barred galaxies are presented. Finally, in Section 5 we present our conclusions.

## 2 The Smaller Alignment Index (SALI)

Let us consider a  $1 - \text{dimensional}$  phase space of a conservative dynamical system, which could be a  $2M - \text{dimensional}$  symplectic map or a Hamiltonian flow of  $N$  degrees of freedom, with  $1 = 2N$ . We consider also an orbit in this space with initial condition  $S(0) = (x_1(0); x_2(0); \dots; x_1(0))$  and two

deviation vectors  $V_1(0) = (dx_{11}(0); dx_{12}(0); \dots; dx_{11}(0))$  and  $V_2(0) = (dx_{21}(0); dx_{22}(0); \dots; dx_{21}(0))$ , from the initial point  $S(0)$ .

For the computation of the SALI of a given orbit, one has to follow the time evolution of the orbit itself and also of two deviation vectors which initially point in two different directions. The evolution of an orbit of a map  $F$  is described by the discrete-time equations of the map:

$$S(n+1) = F(S(n)); \quad (1)$$

where  $S(n) = (x_1(n); x_2(n); \dots; x_l(n))$ , represents the orbit's coordinates at the  $n$ -th iteration. The evolution of the deviation vectors  $V_1(n); V_2(n)$ , in this case, is given by the equations of the tangent map:

$$V(n+1) = D F(S(n)) \quad V(n); \quad (2)$$

In the case of Hamiltonian flows the evolution of an orbit is given by Hamilton's equations of motion:

$$\frac{dS(t)}{dt} = F(S(t)); \quad (3)$$

where  $F$  is a set of  $n$ -functions  $(F_1; F_2; \dots; F_n)$ , while the corresponding evolution of the deviation vectors  $V_1(t); V_2(t)$ , is given by the variational equations:

$$\frac{dV(t)}{dt} = D F(S(t)) \quad V(t); \quad (4)$$

We note that in (2) and (4)  $D F$  denotes the Jacobian matrix of equations (1) and (3) respectively, evaluated at the points of the orbit under study.

At every time step (or iteration) the two deviation vectors  $V_1(t)$  and  $V_2(t)$  are normalized with norm equal to 1 and the SALI is then computed as:

$$SALI(t) = \min \left\{ \frac{V_1(t)}{kV_1(t)k} + \frac{V_2(t)}{kV_2(t)k}, \frac{V_1(t)}{kV_1(t)k} - \frac{V_2(t)}{kV_2(t)k} \right\}; \quad (5)$$

where  $k$  denotes the usual Euclidean norm and  $t$  is the continuous or discrete time.

SALI has a completely different behavior for regular and chaotic orbits and this allows us to clearly distinguish between them. In the case of Hamiltonian flows or  $2M$ -dimensional symplectic maps with  $2M > 2$ , the SALI fluctuates around a non-zero value for regular orbits, while it tends exponentially to zero for chaotic orbits [1, 4, 5], following a rate which depends on the difference of the two largest Lyapunov Exponents [6]. Thus, in 2D and 3D Hamiltonian systems the distinction between ordered and chaotic motion is easily done. On the other hand, in the case of 2D maps the SALI tends to zero both for regular and for chaotic orbits, following however completely different rates, which again allows us to distinguish between the two cases [1].

### 3 Global dynamics of 2D and 4D standard map

As a simple 2D map which exhibits regular and chaotic behavior, we consider the well-known standard map [9] in the form

$$\begin{aligned} x_{n+1} &= x_n + y_{n+1} & (n \text{ odd}) \\ y_{n+1} &= y_n + \frac{K}{2} \sin(2\pi x_n) \end{aligned} \quad (6)$$

where  $K$  is the so-called non-linear parameter of the system.

Before studying the global dynamics of map (6) let us examine in more detail the behavior of SALI for regular and chaotic orbits of a 2D map. In the case of a chaotic orbit, any two deviation vectors will be aligned to the direction defined by the largest Lyapunov exponent  $L_1$ , and consequently SALI tends to zero following an exponential decay of the form  $SALI / e^{2L_1 n}$ , with  $n$  being the number of iterations [6]. In the case of regular orbits any two deviation vectors tend to fall on the tangent space of the torus on which the motion lies [1, 4, 18]. For a 2D map this torus is an 1-dimensional invariant curve, whose tangent space is also 1-dimensional and consequently any two deviation vectors will become aligned. Thus, even in the case of regular orbits in 2D maps the SALI tends to zero. This decay follows a power law [1] having the form  $SALI / 1=n^2$  [18].

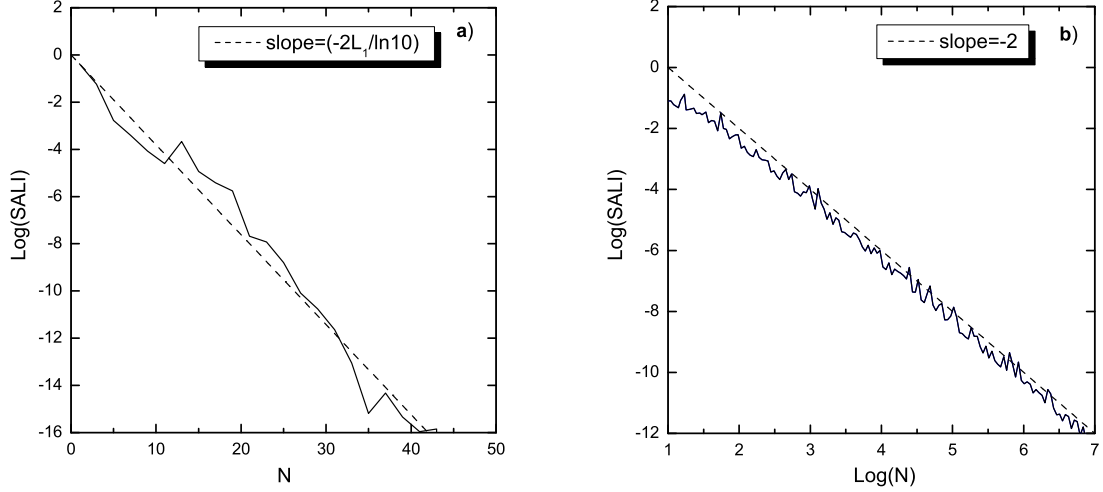


Figure 1: The evolution of SALI (solid lines) for a) the chaotic orbit with initial condition  $x_0 = 0.2, y_0 = 0.2$  and b) the regular orbit with initial condition  $x_0 = 0.4, y_0 = 0.8$  of the standard map (6) for  $K = 2$ , with respect to the number of iterations  $n$ . Note the different scales of the horizontal axis. The Lyapunov exponent of the chaotic orbit is  $L_1 = 0.438$ . Dashed curves in panels a) and b) correspond to functions proportional to  $e^{-2L_1 n}$  and  $1 = n^2$  respectively. It is evident that the theoretical predictions for the evolution of SALI describe very well the numerical data.

In figure 1 we see the different behavior of SALI for regular and chaotic orbits of the standard map (6). It is exactly this different behavior of the index that allows us to use SALI for a fast and clear distinction between regions of chaos and order in the 2-dimensional phase space of the standard map. From the results of figure 1 and the theoretical predictions for the evolution of SALI we see that after  $n = 500$  iterations the value of SALI of a regular orbit becomes of the order of  $10^{-6}$ , while for a chaotic orbit SALI has already reached extremely small values. Thus, the percentage of chaotic orbits for a given value of  $K$  can be computed as follows: We follow the evolution of orbits whose initial conditions lie on a 2-dimensional grid of  $1000 \times 1000$  equally spaced points on the 2-dimensional phase space of the map (dividing in this way the  $(x; y)$  plane in  $10^6$  squares) and register for each orbit the value of SALI after  $n = 500$  iterations. All orbits having values of SALI significantly smaller than  $10^{-6}$  (which correspond to the value SALI reaches after 500 iterations in the case of regular orbits), are characterized as chaotic. In practice as a good threshold for this distinction we consider the value  $10^{-8}$ . Thus, all orbits having SALI  $< 10^{-8}$  after  $n = 500$  iterations are characterized as chaotic, while all others are considered as non-chaotic.

In figure 2a) we present the outcome of this procedure for  $K = 2$ . Each initial condition is colored according to the color scale seen at the right side of the panel. So, chaotic orbits, having SALI  $< 10^{-8}$  are colored black, while light gray color corresponds to regular orbits having high values of SALI. Thus, in figure 2a) we can clearly identify even tiny regions of regular motion which are not easily seen in phase space portraits of the map (figure 2b)).

Using the above-described method we were able to compute very fast and accurately the percentages of regular motion for large values of parameter  $K$ . In figure 3a) we plot the percentage of regular orbits for  $180 \leq K \leq 200$  where  $K$  varies with a step  $K = 0.001$ . A blow-up of the peak appearing close to  $K = 188$  is seen in figure 3b). In order to accelerate the numerical computation we applied the following technique: For each orbit we compute its SALI value at  $n = 500$ , keeping also track of the squares on the  $(x; y)$  plane that the orbit visits in its evolution. Then, we attribute the same SALI value to all these squares. In this way we gain considerably in computational time, since it is not necessary to perform the same computation for the total number of the initial conditions. For each value of  $K$  a grid of  $1000 \times 1000$  initial conditions were used, allowing us to detect extremely tiny regions of regular motion (note that the percentages of regular orbits in figure 3 remain always less than 0.0015%). From the results of figure 3 we see a periodicity of period 2 in the appearance of islands of stability as  $K$  varies, in accordance to the results presented in [20]. In our study we were able to reproduce the results obtained in [20] but with considerably less computational effort. For

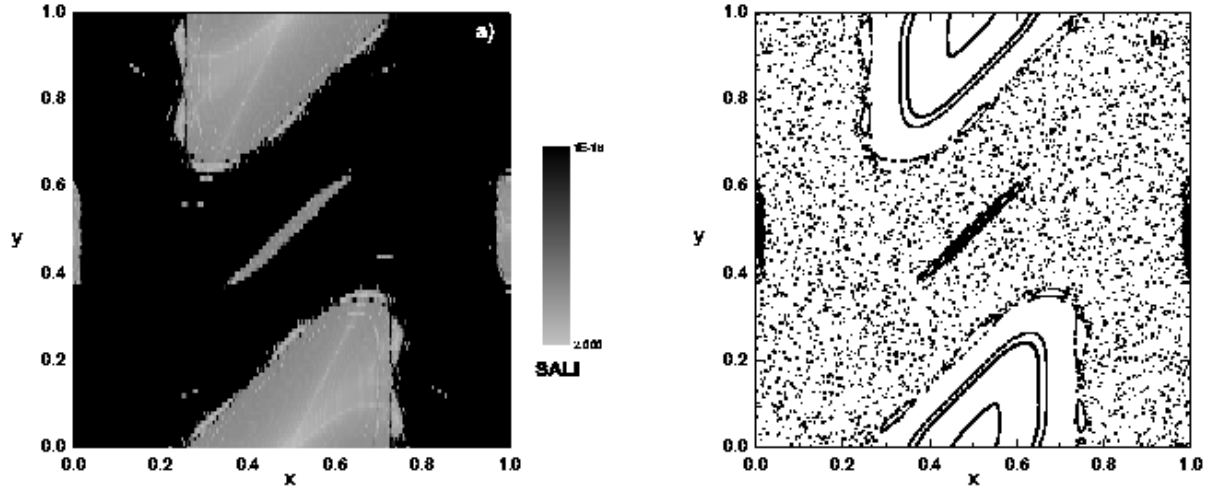


Figure 2: a) Regions of different values of SALI after  $n = 500$  iterations of map (6) for  $K = 2$ . b) Phase space portrait of map (6) for the same value of  $K$ .

example, for  $K = 2$  instead of using all the  $10^6$  initial conditions of the  $1000 \times 1000$  grid, computing the evolution of only 12425 initial conditions up to  $n = 500$  iterations was sufficient for characterizing the total  $10^6$  points. Thus, for  $K = 2$  we were able to compute the percentage of regular orbits on a  $1000 \times 1000$  grid mesh by computation only  $3 \times 500 \times 12425 \times 2 \times 10$  iterations of the map (6) and its tangent map, instead for the  $5 \times 10^6$  iterations needed for obtaining the same result in [20]. In particular for the computation of the data of figure 3 we needed only 27 hours of CPU time on an Athlon 64bit, 3.2GHz PC.

A similar study can be also implemented for the 4D standard map, which is described by the following equations:

$$\begin{aligned} \dot{x}_1^0 &= x_1 + x_2^0 \\ \dot{x}_2^0 &= x_2 + \frac{K}{2} \sin(2x_1) - \sin[2(x_3 - x_1)] \quad (\text{mod } 1) ; \\ \dot{x}_3^0 &= x_3 + x_4^0 \\ \dot{x}_4^0 &= x_4 + \frac{K}{2} \sin(2x_3) - \sin[2(x_1 - x_3)] \end{aligned} \quad (7)$$

where  $K$  is again the nonlinear parameter and the so-called coupling parameter of the system. In figures 4a),b), we present the evolution of the index both for regular and chaotic orbits, for  $K = 3$  and  $\gamma = 0.1$ . For the regular orbit of figure 4a) SALI fluctuates around to a non-zero value, while for the chaotic orbit of figure 4b) SALI decays exponentially to zero reaching extremely small values after only a few iterations ( $N = 150$ ), following the exponential law:  $\text{SALI} / e^{(L_1 + L_2)n}$ , with  $L_1, L_2$  being the two largest Lyapunov exponents of the orbit.

We were also able to measure the percentages of chaotic and regular orbits for the 4D standard map following a similar procedure to the one used in the case of the 2D map. We considered  $10^6$  initial conditions equally spaced in the 4-dimensional phase space of the system, producing in this way a fine grid of 4-dimensional hypercubes. Noting that in the case of chaotic orbits only a few hundreds of iterations are needed for SALI to reach the numerical accuracy of a computer, i.e.  $\text{SALI} < 10^{-16}$  (in the case of the orbits of figure 4b) 150 iterations were sufficient), we started our computation by integrating orbits for only 500 iterations. For each orbit we also kept track of the 4-dimensional hypercubes it visited in its evolution. If the studied orbit was regular, i.e. its final SALI value was larger than  $10^{-8}$ , its final SALI value was attributed to all the hypercubes visited by the orbit. If, on the other hand, the orbit was characterized as chaotic (i.e. its SALI value became  $< 10^{-8}$ ), the evolution of the orbit (but not the evolution of the variational equations) was extended to 5000 iteration, allowing us to attribute the computed SALI value to many hypercubes. This procedure decreases significantly the CPU time needed for the reliable computation of the percentage of regular motion. In particular for  $K = 3$  and  $\gamma = 0.1$  the percentage of regular motion was found to be 8.7% after only 1 minute of computations with the same computer used in the 2D case.

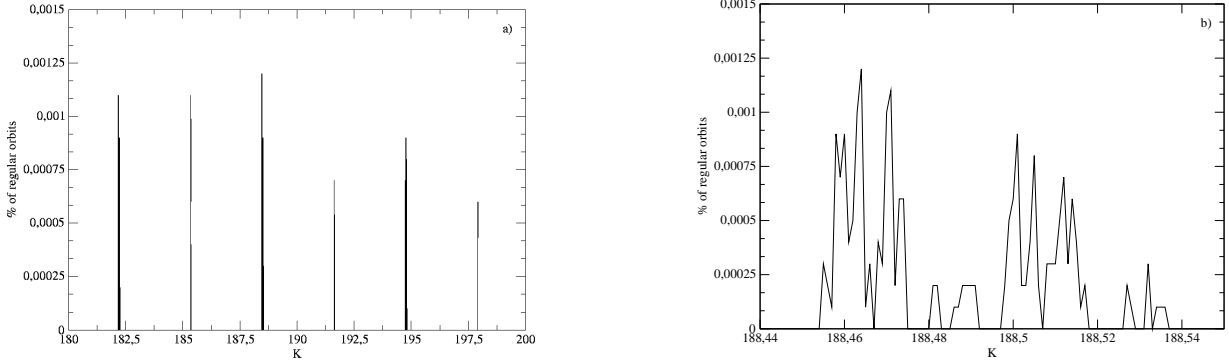


Figure 3: a) Percentages of regular orbits of map (6) as a function of the nonlinear parameter  $K \in [180;200]$ , b) A zoom of panel a) in the region of  $K \in [188.44;188.55]$ .

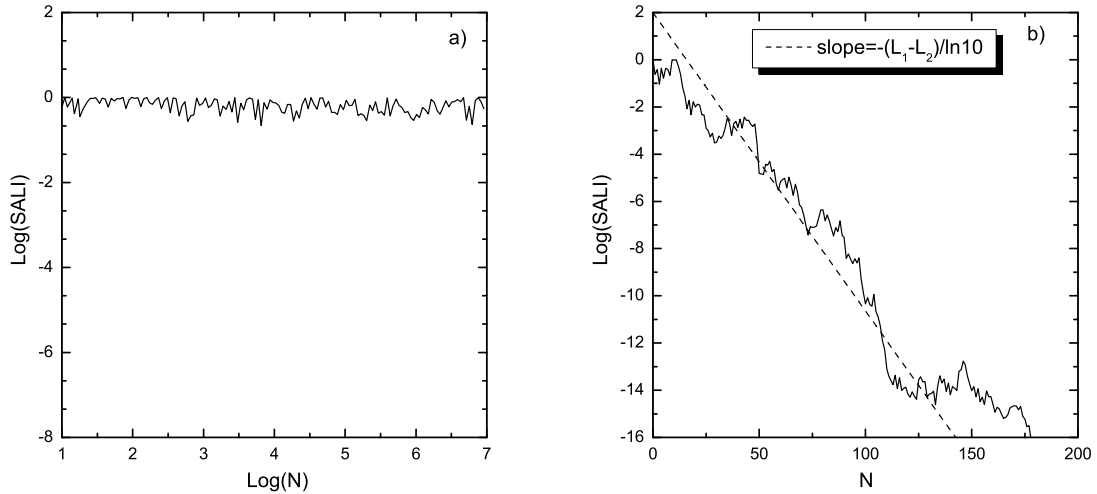


Figure 4: The evolution of the SALI for a) the regular orbit with initial condition  $(x_1; x_2; x_3; x_4) = (0.55; 0.1; 0.62; 0.2)$  and b) the chaotic orbit with initial condition  $(x_1; x_2; x_3; x_4) = (0.55; 0.3; 0.62; 0.2)$  of the 4D standard map with  $K = 3$  and  $\epsilon = 0.1$ . We note that the SALI of the chaotic orbit decays exponentially to zero following the law  $/ e^{-(L_1 - L_2)n}$ .

## 4 Applications to 2D and 3D models of barred galaxies

### 4.1 The model

A 3D rotating model of a barred galaxy can be described by the Hamiltonian function:

$$H = \frac{1}{2} (p_x^2 + p_y^2 + p_z^2) + V(x; y; z) - b(p_y - y p_x); \quad (8)$$

The bar rotates around its  $z$ -axis, while the  $x$ -axis is along the major axis and the  $y$ -axis is along the intermediate axis. The  $p_x; p_y$  and  $p_z$  are the canonically conjugate momenta. Finally,  $V$  is the potential,  $b$  represents the pattern speed of the bar and  $H$  is the total energy of the system.

The potential  $V$  of our model consists of three components:

1. A disc, represented by a Miyamoto disc [21]:

$$V_D = \frac{G M_D}{x^2 + y^2 + (A + \frac{p}{B} z^2 + B^2)^2}; \quad (9)$$

where  $M_D$  is the total mass of the disc,  $A$  and  $B$  are the horizontal and vertical scale lengths, and  $G$  is the gravitational constant.

2. A bulge which is modeled by a Plummer sphere whose potential is:

$$V_S = -\frac{GM_S}{\sqrt{x^2 + y^2 + z^2 + \frac{s^2}{s}}}; \quad (10)$$

where  $s$  is the scalelength of the bulge and  $M_S$  is its total mass.

3. A triaxial Ferrers bar, the density  $(x)$  of which is:

$$(x) = \begin{cases} c(1 - m^2)^2 & ; m < 1 \\ 0 & ; m \geq 1 \end{cases}; \quad (11)$$

where  $c = \frac{105}{32} \frac{GM_B}{abc}$  is the central density,  $M_B$  is the total mass of the bar and

$$m^2 = \frac{x^2}{a^2} + \frac{y^2}{b^2} + \frac{z^2}{c^2}; \quad a > b > c > 0; \quad (12)$$

with  $a, b$  and  $c$  being the semi-axes. The corresponding potential is:

$$V_B = Gabc \frac{c}{n+1} \int_0^{Z^{-1}} \frac{du}{(1 - m^2(u))^{n+1}}; \quad (13)$$

where

$$m^2(u) = \frac{x^2}{a^2 + u} + \frac{y^2}{b^2 + u} + \frac{z^2}{c^2 + u}; \quad (14)$$

$$Z^2(u) = (a^2 + u)(b^2 + u)(c^2 + u); \quad (15)$$

$n$  is positive integer and  $Z$  is the unique positive solution of:

$$m^2(Z) = 1; \quad (16)$$

outside of the bar ( $m = 1$ ), and  $m = 0$  inside the bar.

The corresponding forces are given analytically in [22].

This model has been used extensively for orbital studies [23-27].

## 4.2 Numerical results

We first applied the SALI method to the 2D bar potential resulting from the restriction of our study on the  $z = p_z = 0$  subspace of the whole phase space of the system. It can be easily seen that, due to the symmetries of Hamiltonian (8), orbits starting with  $z = p_z = 0$  remain for all time on the  $(x, y)$  plane. In this case, the Hamiltonian function governing the motion is derived by setting  $z = p_z = 0$  to equations (8)-(15) and the corresponding Poincaré Surface of Section (PSS) is 2-dimensional and can be easily visualized.

As we have already mentioned, in 2D Hamiltonian systems SALI tends exponentially to zero for chaotic orbits, while it fluctuates around a positive number for regular orbits. In figure 5a) we present the PSS (plane  $(y, p_y)$ ) of the system for  $H = 0.360$ , which exhibits both regular and chaotic regions. By choosing orbits with initial conditions on the line  $p_y = 0$  of the PSS and calculating their SALI values at  $t = 3000$  we were able to detect very small regions of stability that can not be visualized easily on the PSS. We plot the corresponding values of the SALI in figure 5b). The values of the SALI tend to zero ( $10^{-16}$ ), for orbits whose initial conditions were chosen inside the chaotic regions of the PSS, contrary to orbits with initial conditions inside the stability islands whose SALI values retain large positive values.

We also used the SALI method to calculate the percentages of regular and chaotic motion for initial conditions chosen on the whole plane  $(y, p_y)$ . For the value of the Hamiltonian function  $E = H = 0.360$  we tested two sets of initial conditions: set A having 5000 initial conditions and set B with 10000 initial conditions. The two sets were used in order to examine the variation of the percentages of the regular and chaotic orbits for different grids of initial conditions. We found that for set A the

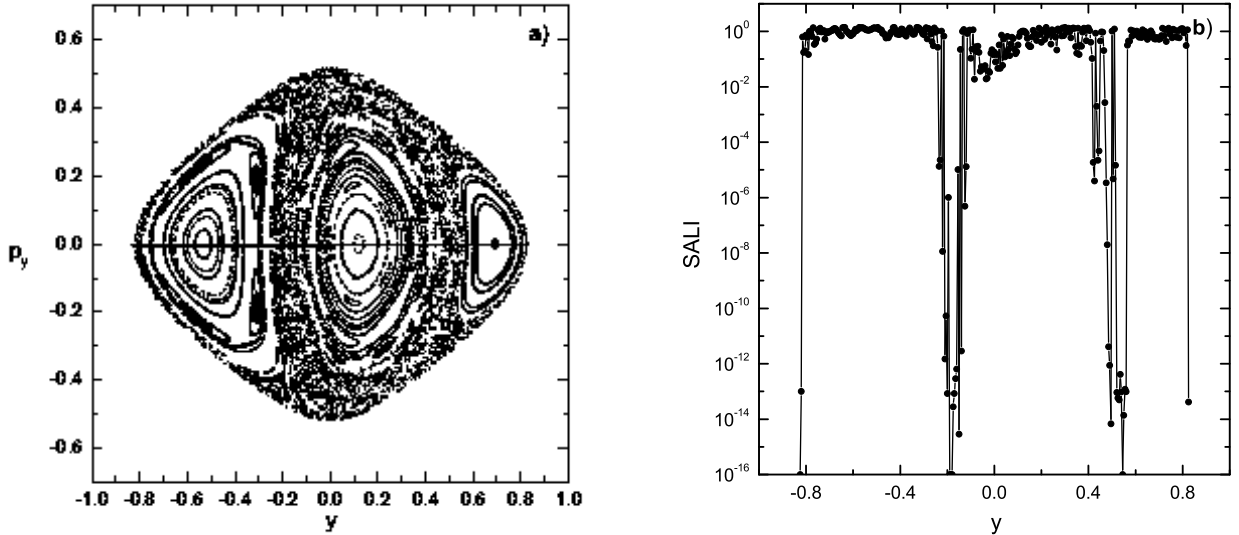


Figure 5: a) Poincaré surface of section for the 2D Ferrers' model in  $(y; p_y)$  plane for  $H = 0.360$ , b) The variation of the SALI value for initial conditions chosen on the line  $p_y = 0$  of the corresponding PSS of panel a).

percentage of chaotic orbits is 22.5%, while for set B 28.0% of the orbits were characterized as chaotic. We note that, as usual, an orbit is considered to be chaotic if its SALI value becomes  $10^{-8}$ . Thus for this particular value of the energy, although a finer grid can help us to detect some small chaotic regions, we can nevertheless derive a good approximation of the real percentage even with a relatively "small" set of initial conditions. Repeating this procedure for several values of the energy, we were able to follow the change of the fraction of chaotic and regular orbits in the phase space as the value of  $H$  varies.

We have also studied the complete 3D model, described by the Hamiltonian (8), for several values of the bar mass  $M_B$  and of the semi minor axis  $c$ . Our basic model (main model), has the following values of parameters:  $G = 1$ ,  $b = 0.054$ ,  $a = 6$ ,  $b = 1.5$ ,  $c = 0.6$ ,  $A = 3$ ,  $B = 1$ ,  $s = 0.4$ ,  $M_B = 0.1$ ,  $M_S = 0.08$ ,  $M_D = 0.82$  both for its 2D and 3D versions. The units used, are: 1 kpc (length), 1 M yr (time),  $2 \cdot 10^{11}$  solar masses (mass). For each model studied we considered two sets of initial conditions. The first set contains orbits with initial conditions in the  $(x; p_x; z)$  space with  $(y; p_y; p_z) = (0; 0; 0)$  and the second one, orbits with initial conditions in the  $(x; p_y; p_z)$  space with  $(y; z; p_x) = (0; 0; 0)$ . Analyzing our numerical results we found that the increase of the bar mass (2GMB - version, with  $M_B = 0.2$ ) introduces more chaotic behavior for both sets of initial conditions. In figure 6 we present the change of percentages of the chaotic orbits as the parameters of Hamiltonian (8) vary for the first set of initial conditions (similar results were also found for the second set). The findings are in accordance to the results obtained in [28] for the 2D case. On the other hand, we discovered that when the bar is thicker, i.e. the length of the z-axis larger (2C - version, with  $c = 1.2$ ), the system becomes less chaotic [11].

Finally, we calculated the percentages of chaotic and regular orbits for different values of the pattern speed  $\omega$ . From the orientation of periodic orbits, Contopoulos [29] showed that bars have to end before corotation, i.e. that  $r_L > a$ , where  $r_L$  the Lagrangian, or corotation, radius. Comparing the shape of the observed dust lanes along the leading edges of bars to that of the shock loci in hydrodynamic simulations of gas flow in barred galaxy potentials, Athanassoula [30, 31] was able to set both a lower and an upper limit to corotation radius, namely  $r_L = (1.2 - 0.2)a$ . This restricts the range of possible values of the pattern speed between a high value that corresponds to the Lagrangian radius  $r_L = 1.4a$  and a low value that corresponds to  $r_L = 1.0a$ . Using the extremes of this range, we investigated how the pattern speed of the bar affects the dynamics of the system and found that the percentage of regular orbits is greater in slow bars [16].

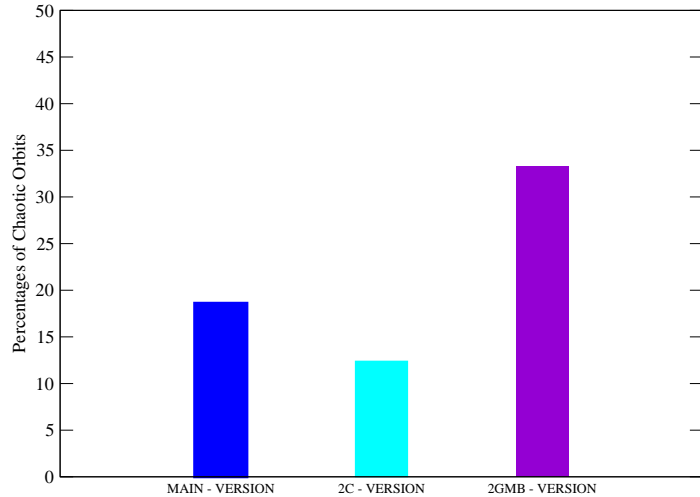


Figure 6: Comparison of the percentages of chaotic orbits for our main galactic model, described by the Hamiltonian function (8) with parameters:  $G = 1$ ,  $b = 0.054$ ,  $a = 6$ ,  $b = 1.5$ ,  $c = 0.6$ ,  $A = 3$ ,  $B = 1$ ,  $s = 0.4$ ,  $M_B = 0.1$ ,  $M_S = 0.08$ ,  $M_D = 0.82$ , a model with twice the length of the short axis  $c = 1.2$  (2C -version) and a model with twice the bar mass  $M_B = 0.2$  (2GMB -version). The system becomes more chaotic as the mass of the bar component increases, while a thicker bar results to the decrease of chaoticity. The initial conditions in this example are given in the  $(x; p_y; z)$  space with  $(y; p_x; p_z) = (0; 0; 0)$

## 5 Conclusions

In this paper, we used the SALI method of chaos detection to study the dynamical behavior of 2 and 4 dimensional symplectic maps and of Hamiltonian models of barred galaxies with 2 and 3 degrees of freedom. Using the SALI we were able to rapidly identify, in the phase spaces of the studied systems, even tiny regions of regular motion and also compute the percentages of regular and chaotic orbits as the values of the parameters of systems vary. In the case of galactic models, we found the influence of some important physical parameters like the mass, the length of the short z-axis and the pattern speed of the bar, on the chaotic behavior of the system. In particular, we found that the growth of the mass of the bar favors the existence of more chaotic orbits, while we observed that by increasing of the length of the short axis of the bar the percentage of the chaotic orbits decreases.

Acknowledgements. We thank the European Social Fund (ESF), Operational Program for Educational and Vocational Training II (EPEAEK II), and particularly the Program PYTHAGORAS II, for funding this work. Visits between the team members were partially funded by the region PACA. T. M. was supported by the "Karatheodory" graduate student fellowship No B 395 of the University of Patras. During his visit in Marseille, his travel and accommodation funds were provided by the Marie Curie fellowship No HPMTC-2001-00338. Ch. Skokos was supported by the Marie Curie Intra-European Fellowship No MEIF-CT-2006-025678. The first author (T. M.) would also like to express his gratitude to the Institut de Mécanique Céleste et de Calcul des Éphémérides (IMCCE) of the Observatoire de Paris for its excellent hospitality during his visit in June 2006, when part of this work was completed.

## References

- [1] Ch. Skokos, J. Phys. A : Math. Gen., 34, 10029, (2001).
- [2] Ch. Skokos, Ch. Antonopoulos, T. Bountis and M. Vrahatis, in Proceedings of the 4th GRACM, ed. D. T. Tsahalis, IV, 1496. (2002).

[3] N. Voglis, C. Kalapotharakos and I. Stavropoulos, *Mon. Not. R. Astron. Soc.*, 337, 619, (2002).

[4] Ch. Skokos, Ch. Antonopoulos, T. Bountis and M. Vrahatis, *Prog. Theor. Phys. Suppl.*, 150, 439, (2003).

[5] Ch. Skokos, Ch. Antonopoulos, T. Bountis and M. Vrahatis, in *Proceedings of the Conference Libration Point Orbits and Applications*, eds. G. Giomaze, M. W. Lo and J. J. M. Asdemont, *World Scientific*, 653, (2003).

[6] Ch. Skokos, Ch. Antonopoulos, T. Bountis and M. Vrahatis, *J. Phys. A*, 37, 6269, (2004).

[7] P. Panagopoulos, T. Bountis and Ch. Skokos, *J. Vib. and Acoust.*, 126, 520, (2004).

[8] A. Szell, B. Erdi, Zs. Sandor and B. Steves, *Mon. Not. R. Astron. Soc.*, 347, 380, (2004).

[9] C. Kalapotharakos, N. Voglis and G. Contopoulos, *Mon. Not. R. Astron. Soc.*, 428, 905, (2004).

[10] Ch. Antonopoulos, T. Manos and Ch. Skokos, in *Proceedings of the 1st IC-SCCE*, ed. D. T. Tsalalis, *Patras Univ. Press*, III, 1082, (2005).

[11] T. Manos and E. Athanassoula, *SF2A-2005: Semaine de l'Astrophysique Francaise*, eds. F. Casoli, T. Contini, J. M. Hameray and L. Paganini, *EDP Sciences Conference Series*, 631, (2005).

[12] T. Manos and E. Athanassoula, *5th International Cosmology Conference: The Fabulous destiny of galaxies: Bridging past and present*, eds. V. Le Brun, A. Masure, S. Amouts, D. Burgarella, *Frontier Group* (2005).

[13] Ch. Antonopoulos and T. Bountis, *Phys. Rev. E*, 73, 056206, (2006).

[14] T. Bountis and Ch. Skokos, *Nucl. Instr. Meth. Phys. Res. (Sect. A)*, 561, 173, (2006).

[15] Ch. Antonopoulos, T. Bountis and Ch. Skokos, *Int. J. Bif. Chaos*, 16 (6), 1777, (2006).

[16] T. Manos and E. Athanassoula, *AIIP Conference Proceedings, Recent Advances in Astronomy and Astrophysics: 7th International Conference of the Hellenic Astronomical Society*, ed. N. Solomos, 848, 662, (2006).

[17] R. Capuzzo-Dolcetta, L. Lecce, D. Merritt and A. Vicari, *astro-ph/0611205*, (2006).

[18] Ch. Skokos, T. Bountis and Ch. Antonopoulos, submitted, (2006).

[19] B. V. Chirikov, *Phys. Rep.*, 52, 265, (1979).

[20] R. Dvorak, B. Funk, F. Freistetter, G. Contopoulos, *Proceedings of the 3rd Austrian-Hungarian Workshop on Trojans and related Topics*, eds. F. Freistetter, R. Dvorak and B. Erdi, 185, (2003).

[21] M. Miyamoto and R. Nagai, *PA SJ*, 27, 533, (1975).

[22] D. Pfenniger, *Astr. Astrophys.*, 134, 373, (1984).

[23] Ch. Skokos, P. A. Patsis and E. Athanassoula, *Mon. Not. R. Astron. Soc.*, 333, 847, (2002).

[24] Ch. Skokos, P. A. Patsis and E. Athanassoula, *Mon. Not. R. Astron. Soc.*, 333, 861, (2002).

[25] P. A. Patsis, Ch. Skokos and E. Athanassoula, *Mon. Not. R. Astron. Soc.*, 337, 578, (2002).

[26] P. A. Patsis, Ch. Skokos and E. Athanassoula, *Mon. Not. R. Astron. Soc.*, 342, 69, (2003).

[27] P. A. Patsis, Ch. Skokos and E. Athanassoula, *Mon. Not. R. Astron. Soc.*, 346, 1031, (2003).

[28] E. Athanassoula, O. Biénamy, L. Martinet and D. Pfenniger, *Astr. Astrophys.*, 127, 349, (1983).

[29] G. Contopoulos, *Astr. Astrophys.*, 81, 198, (1980).

[30] E. Athanassoula, *Mon. Not. R. Astron. Soc.*, 259, 328, (1992).

[31] E. Athanassoula, *Mon. Not. R. Astron. Soc.*, 259, 354, (1992).